Nonlinear valley selection rules and all-optical probe of broken time-reversal symmetry in monolayer WSe$_2$

Paul Herrmann [1], Sebastian Klimmer [1,2], Thomas Lettau[3], Till Weickhardt[1], Anastasios Papavasileiou [4], Kseniia Mosina[4], Zdeněk Sofer[4], Ioannis Paradisanos [5], Daniil Kartashov [6,7], Jan Wilhelm [8,9] & Giancarlo Soavi [1,7] ✉

In monolayer transition metal dichalcogenides, time-reversal symmetry—combined with broken space-inversion symmetry—defines the spin–valley degree of freedom. As such, the engineering and control of time-reversal symmetry by optical or magnetic fields constitutes the foundation of valleytronics. Here we propose a new approach for the detection of broken time-reversal symmetry and valley imbalance in monolayer WSe$_2$ based on second-harmonic generation. At room temperature, our method can selectively probe a net valley imbalance generated by ultrafast, coherent and valley-exclusive optical Stark and Bloch–Siegert effects. This work demonstrates the potential and unique capabilities of nonlinear optics as a probe of broken time-reversal symmetry as well as a tool for ultrafast and non-destructive valleytronic operations.

Time-reversal symmetry (TRS) $E_\uparrow(\mathbf{k}) = E_\downarrow(-\mathbf{k})$ underlies some of the most exotic phases of condensed matter[1]. In monolayer transition metal dichalcogenides (TMDs), the interplay between broken space inversion $E_\uparrow(\mathbf{k}) \neq E_\uparrow(-\mathbf{k})$ and TRS further defines the spin–valley degree of freedom[2,3], where direct transitions in momentum space at the ±K points of the Brillouin zone are energetically degenerate but non-equivalent. Engineering of TRS in TMDs naturally leads to the field of valleytronics, where the degeneracy of ±K valleys is lifted either by magnetic fields (Zeeman splitting)[4] or with circularly polarized light. The latter approach can be further distinguished between the generation of a real exciton population in one of the valleys via one-[5] or two-photon[6] absorption, or by the transient breaking of TRS with coherent processes such as the optical Stark and Bloch–Siegert effects[7,8]. In the vast majority of studies reported so far, the detection of broken TRS

and the consequent valley imbalance has been limited to the realm of linear optics, mainly to the detection of a polarized photoluminescence (PL)[5,9], or the detection of Kerr rotation in the pump–probe configuration to probe valley-polarized resident carriers[10,11] or valley-selective coherent states[7,8]. Both approaches suffer from severe limitations: PL is intrinsically destructive, as it requires the recombination of the electron–hole pair and, thus, the loss of valley information, whereas optical Kerr rotation uses a relatively intense and resonant probe pulse (for example, 100 μW of average power[11]), which can considerably perturb the sample under investigation. Although it is possible to probe a valley imbalance at room temperature[8,12], most experiments on pristine TMDs were performed at cryogenic temperatures, as a shorter exciton lifetime[13] and a longer spin relaxation time[14–16] result in a robust exciton polarization at low temperatures.

[1]Institute of Solid State Physics, Friedrich Schiller University Jena, Jena, Germany. [2]ARC Centre of Excellence for Transformative Meta-Optical Systems, Department of Electronic Materials Engineering, Research School of Physics, The Australian National University, Canberra, Australian Capital Territory, Australia. [3]Institute of Condensed Matter Theory and Optics, Friedrich Schiller University Jena, Jena, Germany. [4]Department of Inorganic Chemistry, University of Chemistry and Technology, Prague, Czech Republic. [5]Institute of Electronic Structure and Laser, Foundation for Research and Technology-Hellas, Heraklion, Greece. [6]Institute of Optics and Quantum Electronics, Friedrich Schiller University Jena, Jena, Germany. [7]Abbe Center of Photonics, Friedrich Schiller University Jena, Jena, Germany. [8]Regensburg Center for Ultrafast Nanoscopy (RUN), University of Regensburg, Regensburg, Germany. [9]Institute of Theoretical Physics, University of Regensburg, Regensburg, Germany. ✉e-mail: giancarlo.soavi@uni-jena.de
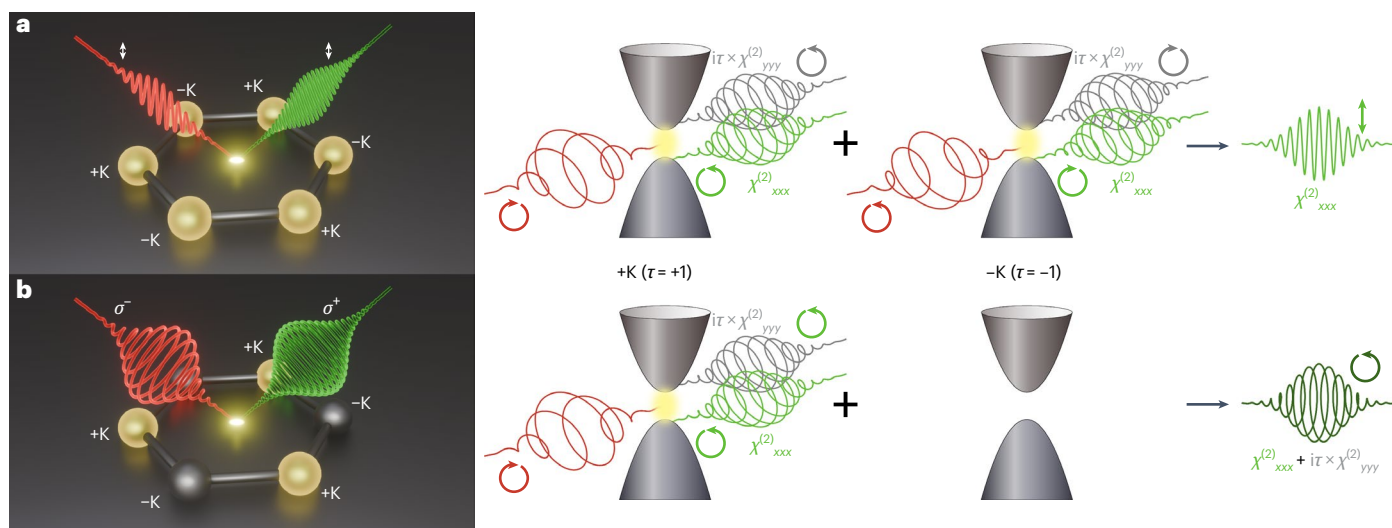
Fig. 1 | Nonlinear valley selection rules in monolayer TMDs. a, A linearly polarized FB (left, red) can be decomposed into right- and left-circular components that interact with the ±K valleys, respectively, emitting counter-rotating SH beams. Since the $\chi^{(2)}_{yyy}$ elements (grey) of the NLO susceptibility cancel out in the two valleys, only the $\chi^{(2)}_{xxx}$ terms (light green) contribute to the emitted signal, which add up again to a linearly polarized SH (right, light green). **b**, A right-circularly polarized FB (left, red) interacts only with the +K valley, and thus, it probes both $\chi^{(2)}_{xxx}$ and $\chi^{(2)}_{yyy}$. Coherent superposition of the two contributions from the +K valley results in circularly polarized SH (right, dark green).

In this context, nonlinear optics (NLO) can provide distinct advantages. An all-optical probe of broken TRS based on NLO has been realized in layered[17] and bulk[18] magnets, as well as in various non-magnetic TMDs under the effect of an external magnetic field[19]. Very recently, ultrafast and room-temperature nonlinear valleytronics has been realized in centrosymmetric materials based on light–matter interactions with engineered topological optical fields[20,21]. In addition, a few theoretical[22–24] and experimental[12,25,26] studies have recently demonstrated the advantages of a detection scheme based on second-harmonic generation (SHG). All these studies were based on the measurement of a rotation in the second-harmonic (SH) polarization ellipse and simultaneously writing the valley state with an elliptically polarized fundamental beam (FB)[12,25,26]. On one hand, this approach clearly surpasses the standard methods based on polarized PL and optical Kerr rotation, because SHG is a parametric process and, thus, ultrafast and non-destructive, especially under the condition in which the SH signal at 2ω is resonant with the exciton transition under investigation. Therefore, the TMD is fully transparent to the FB at ω. On the other hand, the detection of the valley imbalance based on elliptical SHG fails if the polarization of the FB approaches the circular state, because, in this case, there is no well-defined ellipse rotation to measure.

In this work, we experimentally and theoretically study SHG in monolayer WSe$_2$ excited by linearly versus circularly polarized light, and we demonstrate that their ratio can be used as a simple and powerful probe of valley imbalance and broken TRS. Our theoretical model is based on the semiconductor Bloch equations (SBE)[27–30], which we solve both analytically[31] and numerically in the two scenarios where TRS is either preserved (excitation with linearly polarized light) or broken (excitation with circularly polarized light). Broken TRS is included in the model Hamiltonian of monolayer WSe$_2$ as a valley-selective and intensity-dependent perturbation arising from the optical Stark and Bloch–Siegert shifts[7,8]. For a linear FB, the shift in the optical gap is valley symmetric, and thus, TRS is preserved. By contrast, circular excitation leads to valley-exclusive gap opening and TRS breaking, which is reflected in a characteristic modification of the NLO susceptibility. We highlight that our results can provide new insights for understanding previous experiments[12], in which the impact and strength of the optical Stark and Bloch–Siegert effects can be estimated by considering the

energy difference between the fundamental photon energy and the optical gap of the material under investigation. Finally, a key ingredient of our theory and experiments is the observation that some elements of the NLO susceptibility in monolayer TMDs are proportional to the valley index $\tau = \pm 1$, a property that we define as the 'nonlinear valley selection rule'. On the basis of this, we demonstrate that the different polarizations in our SH experiments effectively probe different wave-vector groups[32], and thus, they are subject to different symmetry operations. In particular, SHG with linearly polarized light simultaneously probes both ±K valleys, leading to a cancellation of the terms in the NLO susceptibility that are proportional to τ (Fig. 1a). This leads to a NLO susceptibility that is typical of the D_{3h} point group, corresponding to the wave-vector group at the Γ point of the Brillouin zone for monolayer TMDs. By contrast, SHG with circularly polarized light selectively probes only one of the ±K valleys, and thus, it measures the corresponding C_{3h} wave-vector group (Fig. 1b).

Crystal symmetry and nonlinear valley selection rules

The vast majority of NLO experiments on TMDs[33], such as the measurements of crystal orientation[34], number of layers[35], strain[36] and ultrafast switching[37,38], are based on the assumption that monolayers belong to the D_{3h} point group. However, a closer look shows that the point group (or more precisely the wave-vector group[39]) is D_{3h} only at the Γ point of the Brillouin zone, whereas it is C_{3h} at the ±K points[40]. Thus, resonant excitation of the valleys must be described by the nonlinear elements of the cyclic C_{3h} tensor, rather than those of the dihedral D_{3h} group. The elements of the second-order susceptibility $\chi^{(2)}$ for the C_{3h} point group can be divided into two sub-groups[41], namely, $\chi^{(2)}_{xxx} = -\chi^{(2)}_{xyy} = -\chi^{(2)}_{yyx} = -\chi^{(2)}_{yxy}$ and $\chi^{(2)}_{yyy} = -\chi^{(2)}_{yxx} = -\chi^{(2)}_{xxy} = -\chi^{(2)}_{xyx}$, where x (y) refers to the armchair (zig-zag) axis of the crystal in the case of TMDs. The first subset ($\chi^{(2)}_{xxx}$) is identical to the D_{3h} point group and these elements can fully describe SHG in TMDs in the case of non-resonant excitation (for example, below-gap virtual states), and thus, they represent the crystal (that is, geometrical and intrinsic) response of TMDs. By contrast, the second subset ($\chi^{(2)}_{yyy}$) appears only in the C_{3h} group and must be taken into account in the case of resonant excitation at ±K. To show this, we use analytical expressions of the $\chi^{(2)}$ tensor[31] derived from
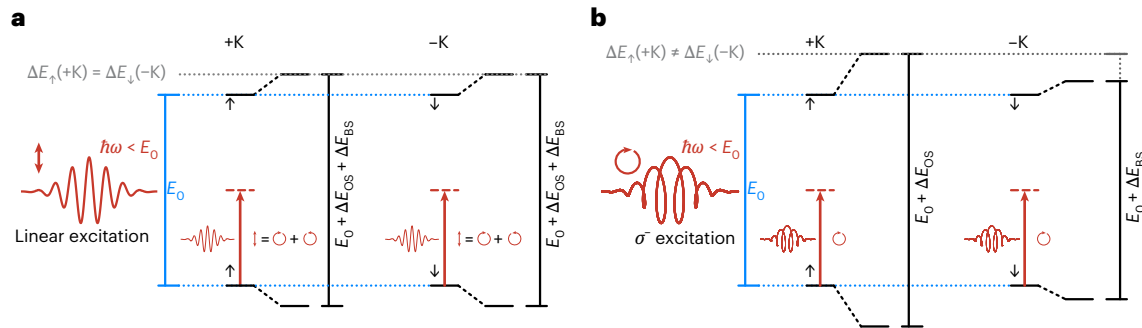
Fig. 2 | TRS breaking by the optical Stark and Bloch–Siegert effects.
a, A linearly polarized FB opens the gap in both valleys by the optical Stark and Bloch–Siegert shifts, interacting equally with the +K and −K valleys. This

preserves TRS, namely, $E_\uparrow(+K) = E_\downarrow(-K)$. **b**, A right-circularly polarized FB opens different gaps by the optical Stark and Bloch–Siegert shifts in the +K and −K valleys, respectively, leading to the breaking of TRS: $E_\uparrow(+K) \neq E_\downarrow(-K)$.

the perturbative solutions of SBEs. In the SBE framework, a monolayer TMD is described by a Hamiltonian, and we use the simplified TMD two-band model valid close to ±K (ref. [42]):

$$h_1(\mathbf{k}) = \begin{pmatrix} \Delta & \gamma^* f^*(\mathbf{k}) \\ \gamma f(\mathbf{k}) & -\Delta \end{pmatrix} \qquad (1)$$

with the on-site energy Δ, effective hopping γ and

$$f(\mathbf{k}) = -i(\kappa_x - i\kappa_y\tau) + \zeta(\kappa_x + i\kappa_y\tau)^2, \qquad (2)$$

where $\kappa_\alpha = a(k_\alpha - K_\alpha)$ is the dimensionless wave vector measured with respect to ±K, a is the TMD lattice constant, $\tau = \pm 1$ is the valley index and ζ is the prefactor of the trigonal warping term, responsible for space inversion breaking. From $h_1(\mathbf{k})$, we calculate the second-order susceptibility contribution from each valley τ as (Supplementary Section 2.2.3)

$$\chi_{xxx}^{(2)}(\tau) = 2\,C\,\frac{a^3|\gamma|^2\zeta}{\Delta^3} = \chi_0^{(2)}, \qquad (3)$$

$$\chi_{yyy}^{(2)}(\tau) = i\tau\chi_0^{(2)}, \qquad (4)$$

where $\chi_{xxx}^{(2)}(\tau) = -\chi_{xyy}^{(2)}(\tau) = -\chi_{yyx}^{(2)}(\tau) = -\chi_{yxy}^{(2)}(\tau)$ and $\chi_{yyy}^{(2)}(\tau) = -\chi_{yxx}^{(2)}(\tau) = -\chi_{xxy}^{(2)}(\tau) = -\chi_{xyx}^{(2)}(\tau)$. Here $C = \frac{\check{c}q}{2\Delta - i/T_2 - 2\omega}$ accounts for the usual resonance condition (Supplementary Section 2.2.3). Note that throughout this work, we use the convention of $\hbar = 1$. We highlight that $\chi_{yyy}^{(2)}(\tau)$ is linear in τ, and thus, it disappears when simultaneously probing both valleys, namely, when the FB is linearly polarized (Fig. 1a). In this condition, the second-order polarization is given as follows.

$$\begin{pmatrix} P_x^{(2)} \\ P_y^{(2)} \end{pmatrix} = \epsilon_0 \sum_{\tau=\pm1} \begin{pmatrix} \chi_{xxx}^{(2)}(\tau) & -\chi_{xxx}^{(2)}(\tau) & -\chi_{yyy}^{(2)}(\tau) \\ -\chi_{yyy}^{(2)}(\tau) & \chi_{yyy}^{(2)}(\tau) & -\chi_{xxx}^{(2)}(\tau) \end{pmatrix} \cdot \begin{pmatrix} E_x^2 \\ E_y^2 \\ 2E_xE_y \end{pmatrix} \qquad (5)$$

$$= 2\epsilon_0 \begin{pmatrix} \chi_0^{(2)} & -\chi_0^{(2)} & 0 \\ 0 & 0 & -\chi_0^{(2)} \end{pmatrix} \cdot \begin{pmatrix} E_x^2 \\ E_y^2 \\ 2E_xE_y \end{pmatrix} \qquad (6)$$

We stress that in equation (6), only the valley-summed susceptibilities $\chi_{xxx}^{(2)} = -\chi_{xyy}^{(2)} = -\chi_{yyx}^{(2)} = -\chi_{yxy}^{(2)} = 2\chi_0^{(2)}$ survive, leading to the typical second-order tensor of the D_{3h} point group[41] and in agreement with the vast majority of reports on SHG in monolayer TMDs[33–37]. This feature is even captured by our numerical simulations (Supplementary Section 2).

In addition, from equations (3) and (4), we stress that (1) $\chi_0^{(2)}$ is directly proportional to the trigonal warping prefactor ζ; (2) the $\chi_{xxx}^{(2)}(\tau)$ and $\chi_{yyy}^{(2)}(\tau)$ terms of the NLO susceptibility are phase shifted by $\pi/2$ at ±K.

If we now move to the circular basis and re-calculate the ±K-resolved NLO susceptibility (Supplementary Section 2.2.4), we obtain

$$\chi_{-++}^{(2)}(\tau) = \sqrt{2}\left(\chi_{xxx}^{(2)}(\tau) + i\chi_{yyy}^{(2)}(\tau)\right) = \sqrt{2}\chi_0^{(2)}(1 - \tau), \qquad (7)$$

$$\chi_{+--}^{(2)}(\tau) = \sqrt{2}\left(\chi_{xxx}^{(2)}(\tau) - i\chi_{yyy}^{(2)}(\tau)\right) = \sqrt{2}\chi_0^{(2)}(1 + \tau), \qquad (8)$$

whereas $\chi_{---}^{(2)}$ and $\chi_{+++}^{(2)}$ vanish. Here the subscripts $\pm$ refer to the helicity of SH polarization and FB. In contrast to the linear case, for circularly polarized SH and FB, the contributions from the ±K valleys towards $\chi_{yyy}^{(2)}$ no longer cancel out (Fig. 1b), and the second-order polarization reads

$$\begin{pmatrix} P_+^{(2)} \\ P_-^{(2)} \end{pmatrix} = \epsilon_0\sqrt{2}\chi_0^{(2)} \sum_{\tau=\pm1} \begin{pmatrix} (1+\tau)E_-^2 \\ (1-\tau)E_+^2 \end{pmatrix} = \epsilon_0 2\sqrt{2}\chi_0^{(2)} \begin{pmatrix} E_-^2 \\ E_+^2 \end{pmatrix}. \qquad (9)$$

In other words, since circularly polarized light selectively probes the valleys, the NLO susceptibility is described by the C_{3h} wave-vector group[41]. In analogy with linear optics, we label the τ proportionality of $\chi_{yyy}^{(2)}$ as the nonlinear valley selection rule, and we stress that this is fundamentally different compared with the selection rules for circularly polarized light based on the conservation of angular momentum[43–45]. The conservation of angular momentum is naturally included in our model in the fact that the elements $\chi_{+++}^{(2)} = \chi_{---}^{(2)} = 0$ and $\chi_{-++}^{(2)} = \chi_{+--}^{(2)} \neq 0$, namely, the observation that a $\sigma_\pm$ FB generates a $\sigma_\mp$ SH.

Finally, we highlight that as long as TRS is preserved, the ratio between the intensities for circularly polarized versus linearly polarized SH is exactly 2, as one can immediately observe by taking the intensity $I \propto |P|^2$ from equations (6) and (9).

TRS breaking in TMDs by off-resonant excitation

We now include TRS breaking into our model Hamiltonian. We do this by considering the optical Stark and Bloch–Siegert shifts[8], namely, by adding an energy shift $\Delta E_{\tau,\sigma} = \frac{|d_{vc}|^2 \mathcal{E}_0^2}{2\Delta + \sigma\tau\omega}$, where we have defined the helicity parameter $\sigma = \pm1$ of the off-resonant FB; the dipole moment $|d_{vc}|$, which is identical at the ±K valley; the FB electric-field strength $\mathcal{E}_0$; and FB frequency ω. Note that the optical Stark and Bloch–Siegert shifts are valley exclusive[7,8]: for instance, a $\sigma = -1$ FB leads to an optical Stark shift of $\Delta E_{+1,-1} = \frac{|d_{vc}|^2\mathcal{E}_0^2}{2\Delta - \omega} = \Delta E_{OS}$ in +K and, simultaneously, to a Bloch–Siegert shift of $\Delta E_{-1,-1} = \frac{|d_{vc}|^2\mathcal{E}_0^2}{2\Delta + \omega} = \Delta E_{BS}$ in −K. In the framework

of perturbative NLO, the optical Stark and Bloch–Siegert effects can also be regarded as a higher-order nonlinear contribution to the emission at the SH photon energy. Thus, the Hamiltonian for broken TRS reads

$$h_2(\mathbf{k}) = \begin{pmatrix} \Delta + \Delta E_{\tau,\sigma} & \gamma^* f^*(\mathbf{k}) \\ \gamma f(\mathbf{k}) & -\Delta - \Delta E_{\tau,\sigma} \end{pmatrix}. \tag{10}$$

The optical Stark and Bloch–Siegert effects shift the bandgap (diagonal elements in equation (10)) of the material[8,46], whereas we do not expect them to change the effective mass of the material (off-diagonal term in equation (10)). We can now calculate the elements of the NLO susceptibility with optical Stark and Bloch–Siegert shifts starting from the model Hamiltonian (equation (10)) (Supplementary Section 2.2.5):

$$\chi_{xxx}^{(2)}(\tau) = \chi_0^{(2)} \left(1 + \frac{4}{3} \frac{|d_{vc}|^2 \mathcal{E}_0^2}{\Delta(2\delta\omega + i/T_2)} \right), \tag{11}$$

$$\chi_{yyy}^{(2)}(\tau) = i\tau\chi_0^{(2)} \left(1 + \frac{4}{3} \frac{|d_{vc}|^2 \mathcal{E}_0^2}{\Delta(2\delta\omega + i/T_2)} \right), \tag{12}$$

where $1/T_2$ is the dephasing rate and we have defined the detuning $\delta\omega = \omega - E_0/2$ using the A1$_s$ exciton resonance energy E_0. Here we observe that $\chi_{xxx}^{(2)}$ is again identical in both valleys ($\tau = \pm1$), and thus, TRS is preserved (Fig. 2a). Therefore, the second-order polarization for a linearly polarized FB becomes

$$\begin{pmatrix} P_x^{(2)} \\ P_y^{(2)} \end{pmatrix} = 2\epsilon_0 \left(1 + \frac{4}{3} \frac{|d_{vc}|^2 \mathcal{E}_0^2}{\Delta(2\delta\omega + i/T_2)} \right) \begin{pmatrix} \chi_0^{(2)} & -\chi_0^{(2)} & 0 \\ 0 & 0 & -\chi_0^{(2)} \end{pmatrix} \cdot \begin{pmatrix} E_x^2 \\ E_y^2 \\ 2E_x E_y \end{pmatrix}, \tag{13}$$

which is, again, the typical expression of the SH for a crystal with D_{3h} symmetry. Finally, we calculate the elements of the NLO susceptibility for circularly polarized light (Supplementary Section 2.2.5), namely, the case in which the gap opening is asymmetric in the two valleys, and thus, TRS is broken (Fig. 2b):

$$\chi_{-++}^{(2)} = 2\sqrt{2}\chi_0^{(2)} \left(1 + \frac{|d_{vc}|^2 \mathcal{E}_0^2}{\Delta(2\delta\omega + i/T_2)} \right) = \chi_{+--}^{(2)}. \tag{14}$$

From this, we derive again the SH polarization as

$$\begin{pmatrix} P_+^{(2)} \\ P_-^{(2)} \end{pmatrix} = \epsilon_0 \, 2\sqrt{2}\chi_0^{(2)} \left(1 + \frac{|d_{vc}|^2 \mathcal{E}_0^2}{2\Delta(\delta\omega + i/T_2)} \right) \begin{pmatrix} E_-^2 \\ E_+^2 \end{pmatrix}. \tag{15}$$

On the basis of equations (11), (12) and (14), TRS breaking can be measured by looking at the ratio η of the SH intensity in the two cases of circular and linear FB polarization:

$$\eta := \frac{I_{\text{circ}}(2\omega)}{I_{\text{lin}}(2\omega)} = \frac{\left| \chi_{+--}^{(2)} \right|^2}{\left| \chi_{xxx}^{(2)} \right|^2}$$

$$= 2 \cdot \frac{\left| 1 + \frac{|d_{vc}|^2 \mathcal{E}_0^2}{\Delta(2\delta\omega + i/T_2)} \right|^2}{\left| 1 + \frac{4}{3} \frac{|d_{vc}|^2 \mathcal{E}_0^2}{\Delta(2\delta\omega + i/T_2)} \right|^2} = 2 \cdot \frac{\left| 1 + \frac{\Delta E_{\text{OS}}}{2\delta\omega + i/T_2} \right|^2}{\left| 1 + \frac{\Delta E_{\text{OS}} + \Delta E_{\text{BS}}}{2\delta\omega + i/T_2} \right|^2}, \tag{16}$$

assuming an equal intensity of incident linearly and circularly polarized FB: $|I_0^{\text{lin}}(\omega)| = |I_0^{\text{circ}}(\omega)|$. If we consider the Taylor expansion of equation (16) up to the first order in $I_0 \propto \mathcal{E}_0^2$, we obtain

$$\eta \cong 2 - \frac{4}{3} \frac{|d_{vc}|^2 \mathcal{E}_0^2}{\Delta} \text{ Re} \left(\frac{1}{2\delta\omega + i/T_2} \right) \cong 2 \left| \frac{1 + \delta_{\text{OS}} - \delta_{\text{BS}}}{1 + \delta_{\text{OS}}} \right|^2, \tag{17}$$

where $\delta_{\text{OS/BS}} = \frac{\Delta E_{\text{OS/BS}}}{(2\delta\omega + i/T_2)}$ (Supplementary Section 2.2.5). As expected, the ratio η depends on the energy difference ($\delta_{\text{OS}} - \delta_{\text{BS}}$) between the ±K valleys, and it tends to 2 if TRS is preserved (that is, in the absence of the valley-asymmetric gap opening). Furthermore, we highlight the dependence $\eta \propto \text{Re} \left(\frac{1}{2\delta\omega + i/T_2} \right)$, which results in a derivative-like shape when crossing the A1$_s$ exciton resonance, as we will show later in our experiments. In addition, η depends on the material parameters (for example, the dipole moment d_{vc} and dephasing time T_2) and experimental parameters (such as the electric-field strength of the FB $\mathcal{E}_0$ and detuning $\delta\omega$). Therefore, even though the effect is enhanced at resonance ($\delta\omega \to 0$), it is possible to observe broken TRS even for off-resonant SHG, whereas the ratio $\eta \to 2$ is only far from resonance, namely, when $\delta\omega \to \infty$.

Experimental and analytical results

To demonstrate the features discussed in the previous section, we perform SH experiments at different wavelengths (SH signal at 690–820 nm, corresponding to an FB in the range of 1,380–1,640 nm) and scan across the A1$_s$ exciton resonance of a monolayer WSe$_2$ sample (Methods provides details on the sample fabrication). First, we performed differential reflectivity $\Delta R/R$ and PL (Fig. 3a), Raman spectroscopy (Fig. 3b) and SH power dependence (Fig. 3c) measurements to confirm the monolayer nature of our sample. One prominent feature arising from the A exciton is observed in the $\Delta R/R$ value. The PL emission is plotted in the same figure for comparison with $\Delta R/R$, and it shows a negligible Stokes shift, indicating the absence of contribution from localized defect states in the material[47]. The Raman spectrum (Fig. 3b) shows the spectrally overlapping E′ and A$_1$′ modes and the second-order 2LA mode. The distance between the two peaks of approximately 11 cm^{-1} is typical of a WSe$_2$ monolayer[48]. Finally, the SH power dependence (Fig. 3c) recorded for an FB of 1,500 nm shows a slope (in log–log scale) of ~2, as expected for SHG. A more detailed analysis of the SH power dependence will be discussed below.

To measure the broken TRS from the ratio η, we tune the ellipticity of the FB (from linear to circular) and detect the total SH intensity (Fig. 3d and Methods provide details on the experimental setup). Figure 3e shows the ellipticity-dependent measurements for three selected wavelengths: at resonance (750 nm) and away from the resonance (780 nm and 720 nm) with respect to the A1$_s$ exciton of our sample. Here the FB power is kept constant at 6 mW. The curves are normalized (that is, we set the SH intensity to 1 for linear excitation) and we paid particular attention to remove any possible contribution from two-photon PL (Supplementary Section 4), which could alter the ratio of the circular/linear SH intensity. Clearly, this ratio is highly dispersive and can dramatically differ from 2 (that is, the ratio expected when TRS is preserved), particularly in the case of resonant SHG. To further highlight this point, in Fig. 4a, we plot the wavelength dependence of η (black squares) on top of the linear PL measured on the same sample (orange curve). This ratio displays values both above and below 2 (horizontal dashed line) in correspondence with the exciton transition. Furthermore, we point out that the ratio η has a clear 'derivative shape' across the A1$_s$ exciton resonance, which arises from the $\frac{1}{\delta\omega}$ dependence of equation (16)/(17). It is worth noting that the ratio η is approximately 2 close to zero detuning ($\delta\omega \approx 0$), even though this wavelength falls in the resonant region in which TRS is broken. We argue that in this case, the fingerprint of broken TRS can be found in the phase difference ($\Delta\phi$) between $\chi_{xxx}^{(2)}$ and $\chi_{+--}^{(2)}$. Our experimental results are in good agreement with the dispersion of the ratio η obtained from our analytical model (16), as plotted in Fig. 4b for dephasing times of $T_2 = 100$ fs, 250 fs and 500 fs and an FB power of 6.5 mW (Supplementary Section 2.2.5). We observe that the depicted data fall within a range of dephasing time of 100–250 fs, which is in excellent agreement with the
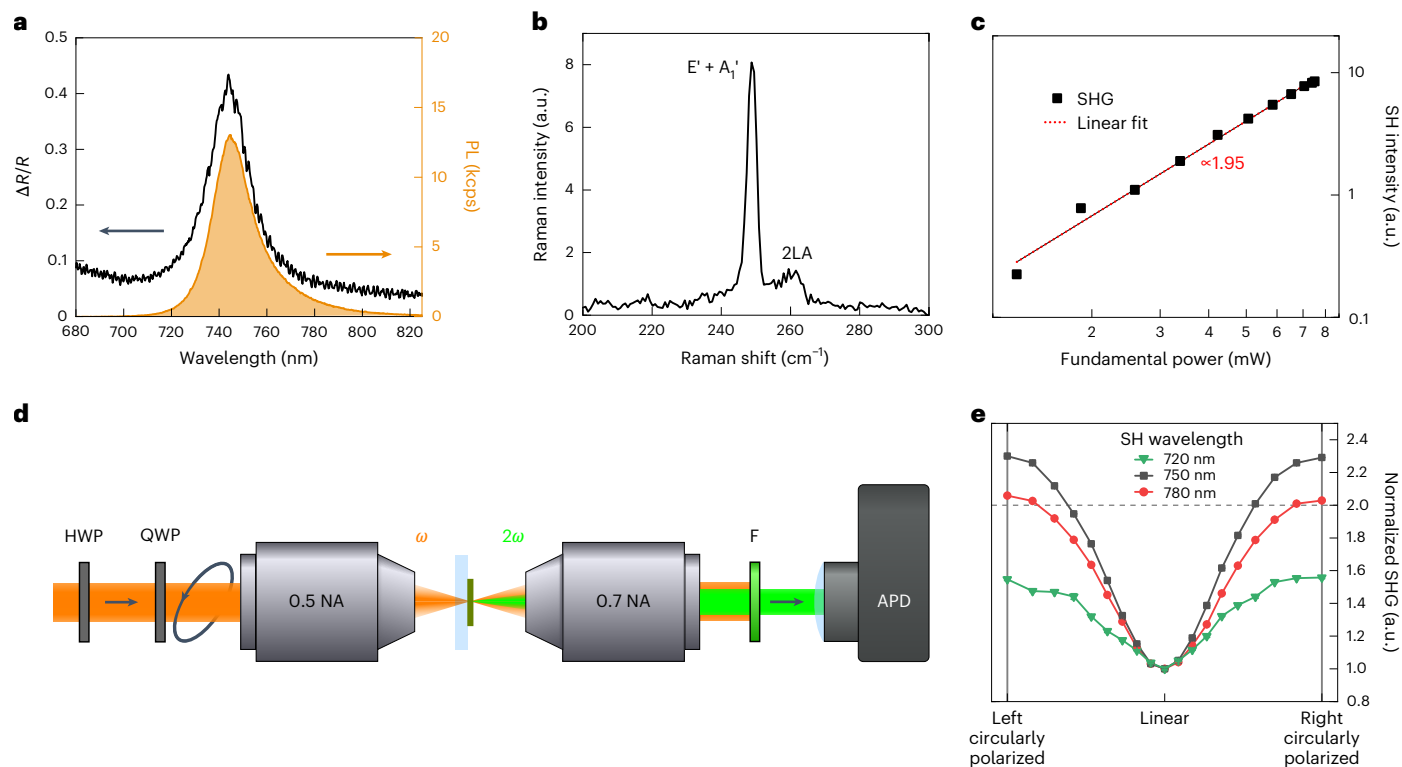
Fig. 3 | Sample characterization and ellipticity-dependent NLO in monolayer WSe$_2$. a, Comparison of PL (orange, right y axis in 10^3 counts per second (kcps)) and $\Delta R/R$ (black, left y axis). **b**, Raman spectrum showing the characteristic E', A$_1'$ and 2LA modes. **c**, Double-logarithmic plot of the SH intensity (black squares) versus the FB power. The linear fit (red dotted line) shows a slope of 1.95. **d**, Experimental setup with the half-wave plate (HWP) and quarter-wave plate (QWP) to control the polarization state of the FB (ω, orange). The emitted SH is filtered (F) and detected by a silicon avalanche photodiode (APD). NA, numerical aperture. **e**, Normalized total emitted SH as a function of the ellipticity of the FB for SH wavelengths of 720 nm (green triangles), 750 nm (red circles) and 780 nm (black squares).
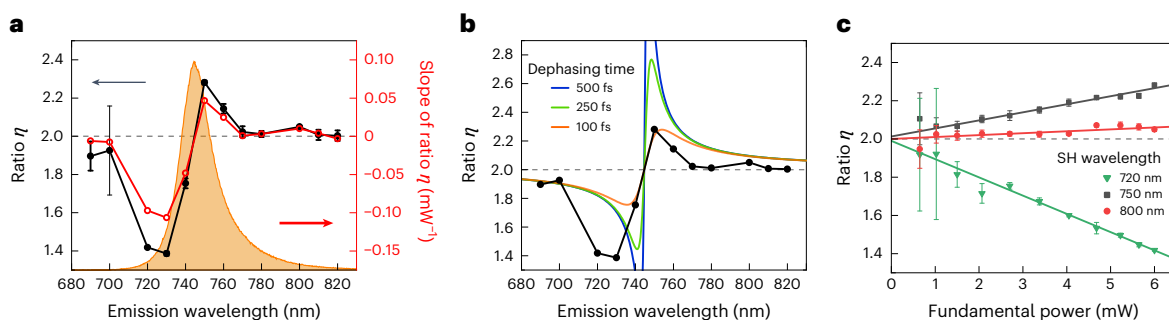
Fig. 4 | Measurement of broken TRS in monolayer WSe$_2$ using circular SHG. a, PL (orange curve) superimposed onto the SH ratio η (black closed circles, left y axis) for an excitation power of 6 mW, and to the slope of η (red open circles, right y axis) for different wavelengths across the exciton resonance. **b**, Comparison of the analytically calculated wavelength dependence of η from equation (16)
(excitation power of 6.5 mW and dephasing times T_2 = 100 fs, 250 fs and 500 fs, with $|d_{vc}|$ = 6 eÅ and $\Delta = E_0/2 = 0.83$ eV) and the experimental data from **a** (black closed circles). **c**, Power dependence of η for SH wavelengths of 720 nm (green triangles), 750 nm (black squares) and 800 nm (red circles).

expected value of dephasing time at room temperature from electron–phonon scattering at the ±K points[49]. Finally, we stress that the influence of the dephasing time T_2 is a direct consequence of considering a monochromatic field within our theoretical model.

In addition, Fig. 4c shows the power dependence of η for three example SH wavelengths (720 nm, 750 nm and 800 nm). The SH ratio η tends to 2 when the FB power tends to 0, namely, when TRS is preserved in the absence of an external perturbation. Moreover, the ratio η shows a linear power dependence with respect to the FB, in agreement with our analytical results from equation (17). This linear power dependence is a natural consequence of the fact that TRS is broken by the coherent optical Stark and Bloch–Siegert effects. Figure 4a also shows the slope of η (red open circles), obtained from a linear fit of all the wavelengths

investigated in our experiments (Supplementary Fig. 5), displaying exactly the same derivative shape of the ratio η at a fixed FB power.

Finally, we highlight that with our analytical model, we can estimate the optical Stark ($\sigma\tau = -1$) and Bloch–Siegert ($\sigma\tau = 1$) shifts as

$$\Delta E_{\tau,\sigma} = \frac{|d_{vc}|^2 \mathcal{E}_0^2}{2\Delta + \sigma\tau\omega}$$ using the parameters shown in Fig. 4. For an excitation wavelength of 1,500 nm, we obtain a gap opening of 17 meV and 6 meV from the optical Stark and Bloch–Siegert shifts, respectively. On rescaling by the input power and detuning, these values are in reasonable agreement with previously reported values[7,8] (Supplementary Section 3). Thus, the agreement between experiments and theory (without any fitting parameter) demonstrates the capability of our detection scheme to quantitatively measure broken TRS in monolayer TMDs.

Discussion

We established a new method based on circular SHG to probe the valley degree of freedom in TMDs, and more generally, to probe broken TRS in crystals belonging to the D_{3h} point group. We demonstrate that the NLO response of TMD monolayers must be interpreted looking at the wave-vector group, rather than the point group. Furthermore, with our analytical model, we clarify the origin of the different wave-vector groups that describe circular and linear excitations, and attribute this difference to the nonlinear valley selection rule. Finally, we analytically derive and experimentally show that the coherent and off-resonant optical Stark effect and Bloch–Siegert shift break TRS, and their effects can be measured by simply looking at the ratio η between the SH intensities emitted from circularly and linearly polarized FBs. Building on this, our approach can be used as a powerful detection scheme for valleytronic operations. This could be done, for instance, by selecting the SH wavelength with the largest slope of η as a function of power. Subsequently, TRS can be controlled with external knobs, such as the valley Zeeman splitting using magnetic fields[50] or by generating a net valley polarization using one-photon absorption with circularly polarized light[51]. Finally, the broken TRS can be measured with our method by looking at the changes in the ratio η with and without the presence of external perturbations. Thus, this work demonstrates the unique capabilities of NLO as an ultrafast and non-invasive probe of broken TRS and of the valley degree of freedom in TMDs.

Online content

Any methods, additional references, Nature Portfolio reporting summaries, source data, extended data, supplementary information, acknowledgements, peer review information; details of author contributions and competing interests; and statements of data and code availability are available at https://doi.org/10.1038/s41566-024-01591-z.

References

1. Sato, M. & Ando, Y. Topological superconductors: a review. *Rep. Progr. Phys.* **80**, 076501 (2017).
2. Liu, G.-B., Xiao, D., Yao, Y., Xu, X. & Yao, W. Electronic structures and theoretical modelling of two-dimensional group-VIB transition metal dichalcogenides. *Chem. Soc. Rev.* **44**, 2643–2663 (2015).
3. Vitale, S. A. et al. Valleytronics: opportunities, challenges, and paths forward. *Small* **14**, 1801483 (2018).
4. MacNeill, D. et al. Breaking of valley degeneracy by magnetic field in monolayer MoSe$_2$. *Phys. Rev. Lett.* **114**, 037401 (2015).
5. Mak, K. F., He, K., Shan, J. & Heinz, T. F. Control of valley polarization in monolayer MoS$_2$ by optical helicity. *Nat. Nanotechnol.* **7**, 494–498 (2012).
6. Wang, G. et al. Giant enhancement of the optical second-harmonic emission of WSe$_2$ monolayers by laser excitation at exciton resonances. *Phys. Rev. Lett.* **114**, 097403 (2015).
7. Kim, J. et al. Ultrafast generation of pseudo-magnetic field for valley excitons in WSe$_2$ monolayers. *Science* **346**, 1205–1208 (2014).
8. Sie, E. J. et al. Large, valley-exclusive Bloch-Siegert shift in monolayer WS$_2$. *Science* **355**, 1066–1069 (2017).
9. Zeng, H., Dai, J., Yao, W., Xiao, D. & Cui, X. Valley polarization in MoS$_2$ monolayers by optical pumping. *Nat. Nanotechnol.* **7**, 490–493 (2012).
10. Yang, L. et al. Long-lived nanosecond spin relaxation and spin coherence of electrons in monolayer MoS$_2$ and WS$_2$. *Nat. Phys.* **11**, 830–834 (2015).
11. Hsu, W.-T. et al. Optically initialized robust valley-polarized holes in monolayer WSe$_2$. *Nat. Commun.* **6**, 8963 (2015).
12. Herrmann, P. et al. Nonlinear all-optical coherent generation and read-out of valleys in atomically thin semiconductors. *Small* **19**, 2301126 (2023).
13. Lagarde, D. et al. Carrier and polarization dynamics in monolayer MoS$_2$. *Phys. Rev. Lett.* **112**, 047401 (2014).
14. Paradisanos, I. et al. Prominent room temperature valley polarization in WS$_2$/graphene heterostructures grown by chemical vapor deposition. *Appl. Phys. Lett.* **116**, 203102 (2020).
15. Glazov, M. M. et al. Spin and valley dynamics of excitons in transition metal dichalcogenide monolayers. *Phys. Status Solidi B* **252**, 2349–2362 (2015).
16. Wang, Z. et al. Intravalley spin–flip relaxation dynamics in single-layer WS$_2$. *Nano Lett.* **18**, 6882–6891 (2018).
17. Sun, Z. et al. Giant nonreciprocal second-harmonic generation from antiferromagnetic bilayer CrI$_3$. *Nature* **572**, 497–501 (2019).
18. Fiebig, M., Fröhlich, D., Krichevtsov, B. & Pisarev, R. V. Second harmonic generation and magnetic-dipole-electric-dipole interference in antiferromagnetic Cr$_2$O$_3$. *Phys. Rev. Lett.* **73**, 2127 (1994).
19. Wu, S. et al. Extrinsic nonlinear Kerr rotation in topological materials under a magnetic field. *ACS Nano* **17**, 18905–18913 (2023).
20. Mitra, S. et al. Light-wave-controlled Haldane model in monolayer hexagonal boron nitride. *Nature* **628**, 752–757 (2024).
21. Tyulnev, I. et al. Valleytronics in bulk MoS$_2$ with a topologic optical field. *Nature* **628**, 746–751 (2024).
22. Wehling, T. O., Huber, A., Lichtenstein, A. I. & Katsnelson, M. I. Probing of valley polarization in graphene via optical second-harmonic generation. *Phys. Rev. B* **91**, 041404 (2015).
23. Cheng, J. et al. Chiral selection rules for multi-photon processes in two-dimensional honeycomb materials. *Opt. Lett.* **44**, 2141–2144 (2019).
24. Hipolito, F. & Pereira, V. M. Second harmonic spectroscopy to optically detect valley polarization in 2D materials. *2D Mater.* **4**, 021027 (2017).
25. Ho, Y. W. et al. Measuring valley polarization in two-dimensional materials with second-harmonic spectroscopy. *ACS Photonics* **7**, 925–931 (2020).
26. Mouchliadis, L. et al. Probing valley population imbalance in transition metal dichalcogenides via temperature-dependent second harmonic generation imaging. *npj 2D Mater. Appl.* **5**, 6 (2021).
27. Schmitt-Rink, S., Chemla, D. S. & Haug, H. Nonequilibrium theory of the optical Stark effect and spectral hole burning in semiconductors. *Phys. Rev. B* **37**, 941–955 (1988).
28. Lindberg, M. & Koch, S. W. Effective Bloch equations for semiconductors. *Phys. Rev. B* **38**, 3342–3350 (1988).
29. Wilhelm, J. et al. Semiconductor Bloch-equations formalism: derivation and application to high-harmonic generation from Dirac fermions. *Phys. Rev. B* **103**, 125419 (2021).
30. Yue, L. & Gaarde, M. B. Introduction to theory of high-harmonic generation in solids: tutorial. *J. Opt. Soc. Am. B* **39**, 535–555 (2022).
31. Aversa, C. & Sipe, J. E. Nonlinear optical susceptibilities of semiconductors: results with a length-gauge analysis. *Phys. Rev. B* **52**, 14636–14645 (1995).
32. Zhang, Y. et al. Chirality logic gates. *Sci. Adv.* **8**, eabq8246 (2022).
33. Dogadov, O., Trovatello, C., Yao, B., Soavi, G. & Cerullo, G. Parametric nonlinear optics with layered materials and related heterostructures. *Laser Photonics Rev.* **16**, 2100726 (2022).
34. Malard, L. M., Alencar, T. V., Barboza, A. P. M., Mak, K. F. & de Paula, A. M. Observation of intense second harmonic generation from MoS$_2$ atomic crystals. *Phys. Rev. B* **87**, 201401 (2013).
35. Li, Y. et al. Probing symmetry properties of few-layer MoS$_2$ and h-BN by optical second-harmonic generation. *Nano Lett.* **13**, 3329–3333 (2013).

36. Mennel, L. et al. Optical imaging of strain in two-dimensional crystals. *Nat. Commun.* **9**, 516 (2018).

37. Klimmer, S. et al. All-optical polarization and amplitude modulation of second-harmonic generation in atomically thin semiconductors. *Nat. Photonics* **15**, 837–842 (2021).

38. Sinelnik, A. et al. Ultrafast all-optical second harmonic wavefront shaping. *Nat. Commun.* **15**, 2507 (2024).

39. Dresselhaus, M., Dresselhaus, G. & Jorio, A. *Group Theory: Application to the Physics of Condensed Matter* (Springer, 2007).

40. Fajardo, E. & Winkler, R. Effective dynamics of two-dimensional bloch electrons in external fields derived from symmetry. *Phys. Rev. B* **100**, 125301 (2019).

41. Boyd, R. W. *Nonlinear Optics* (Academic Press, 2020).

42. Taghizadeh, A. & Pedersen, T. G. Nonlinear optical selection rules of excitons in monolayer transition metal dichalcogenides. *Phys. Rev. B* **99**, 235433 (2019).

43. Bloembergen, N. Conservation laws in nonlinear optics. *J. Opt. Soc. Am.* **70**, 1429–1436 (1980).

44. Simon, H. J. & Bloembergen, N. Second-harmonic light generation in crystals with natural optical activity. *Phys. Rev.* **171**, 1104–1114 (1968).

45. Tang, C. L. & Rabin, H. Selection rules for circularly polarized waves in nonlinear optics. *Phys. Rev. B* **3**, 4025–4034 (1971).

46. Slobodeniuk, A. O. et al. Ultrafast valley-selective coherent optical manipulation with excitons in WSe_2 and MoS_2 monolayers. *npj 2D Mater. Appl.* **7**, 17 (2023).

47. Paradisanos, I. et al. Efficient phonon cascades in WSe_2 monolayers. *Nat. Commun.* **12**, 538 (2021).

48. Sahin, H. et al. Anomalous Raman spectra and thickness-dependent electronic properties of WSe_2. *Phys. Rev. B* **87**, 165409 (2013).

49. Korolev, V. et al. Unveiling the role of electron-phonon scattering in dephasing high-order harmonics in solids. Preprint at https://arxiv.org/abs/2401.12929v1 (2024).

50. Srivastava, A. et al. Valley Zeeman effect in elementary optical excitations of monolayer WSe_2. *Nat. Phys.* **11**, 141–147 (2015).

51. Ye, Z., Sun, D. & Heinz, T. F. Optical manipulation of valley pseudospin. *Nat. Phys.* **13**, 26–29 (2017).

Methods

Fabrication of bulk crystals

The synthesis of WSe_2 was performed by chemical vapour transport in a quartz glass ampoule from tungsten (99.999%; 100 mesh, China Rhenium) and selenium (99.9999%, granules of 1–6 mm, Wuhan Xinrong New Material) in stochiometric amounts corresponding to 100 g WSe_2. In addition, excess of 2 at.% selenium, 0.5 g $SeCl_4$ (99.9%, rough crystalline powder, Strem) and 0.5 g iodine (99.9%, granules, Fisher Scientific) were added in a glove box to the ampoule (50×250 mm²; wall thickness, 3 mm) and the ampoule was sealed by an oxygen–hydrogen welding torch under a high vacuum (under 1×10^{-3} Pa) using a diffusion pump with a liquid-nitrogen trap. The sealed ampoule was first placed in a muffle furnace and heated to 500 °C for 25 h, 600 °C for 50 h and finally 800 °C for 50 h. The heating and cooling rates were 1 °C min⁻¹. The ampoule with the formed WSe_2 powder was placed in a two-zone horizontal furnace. First, the growth zone was heated to 1,000 °C and the source zone, to 800 °C. After 2 days, the thermal gradient was reversed, as the source zone was kept at 1,000 °C, whereas the growth zone was kept at 900 °C for 10 days. During cooling, the thermal gradient was reversed for 2 h, to remove the transport medium and volatile compounds. The ampoule was opened in an argon-filled glove box.

Sample preparation and characterization

We mechanically exfoliate a monolayer of WSe_2 from a bulk crystal onto polydimethylsiloxane and transfer it onto a transparent fused silica substrate. The monolayer nature of our sample is confirmed by optical PL, Raman and SHG measurements (Fig. 3a–c).

Polarization-resolved SHG

For the SHG measurements, we use a custom-made multiphoton microscope, which we operate in the transmission geometry (Fig. 3d). The FB is generated by an optical parametric oscillator (Levante IR fs from APE), pumped by the output of an Yb-doped mode-locked laser (FLINT FL2-12, LIGHT CONVERSION) with a repetition rate of 76 MHz and a pulse length of ~100 fs. This allows tuning the FB from 1,300 nm to 2,000 nm. Before entering the microscope, a combination of half-wave plate (AHWP05M-1600, Thorlabs) and quarter-wave plate (#46-562, Edmund Optics), both mounted on motorized rotation mounts (RSP05/M, Thorlabs), allows us to fully control the polarization state of the FB. Subsequently, the FB is focused onto the sample by a ×40 objective (LMM-40X-P01, Thorlabs) and the transmitted FB as well as the generated SH are collimated by a lens (C330TMD, Thorlabs). The transmitted FB is blocked by a shortpass filter (FESH0950, Thorlabs) and the SH is spectrally filtered by bandpass filters. Finally, we detect the SH with a silicon avalanche photodiode (APD440A, Thorlabs) and lock-in amplifier (HF2LI, Zurich Instruments).

Differential reflectivity and PL

Room-temperature differential reflectivity ($\Delta R/R$) measurements are performed using a custom-built confocal microscope. A halogen lamp with a stabilized power supply serves as the white light source for reflectivity, focused on a pinhole that is imaged on the sample. The reflected light is then dispersed in a spectrometer and detected by a Si charge-coupled device camera. The excitation/detection spot diameter is approximately 1 μm, smaller than the typical size of the monolayers. Differential reflectivity is defined as $(R_{sub} - R_{sam})/R_{sub}$, where R_{sam} represents the intensity reflection coefficient of the sample with the WSe_2 monolayers and R_{sub} denotes the same structure without WSe_2. The PL experiments are conducted on the same areas of the monolayer using the same custom-built confocal microscope and a 633 nm He–Ne laser as the excitation source.

Numerical methods

We simulated the SHG using the SBEs[27–30]. The material data are calculated using a two-band tight-binding model[52] fitted to the density functional theory band structure of WSe_2 in the vicinity of the $\pm K$ points of the Brillouin zone. Further details are provided in Supplementary Section 2.1.

Data availability

The data that support the plots within this paper and other findings of this study are available from the corresponding author on reasonable request.

References

52. Chacón, A. et al. Circular dichroism in higher-order harmonic generation: heralding topological phases and transitions in chern insulators. *Phys. Rev. B* **102**, 134115 (2020).

Author contributions

P.H. and G.S. conceived the experiments. P.H., S.K. and T.W. performed the NLO experiments and analysed the data. P.H. and S.K. prepared the monolayer sample by mechanical exfoliation. I.P. performed the linear optical characterization of the sample. T.L. performed the numerical simulations. J.W. developed the theoretical analytical model based on the SBE and supervised the numerical simulations. A.P., K.M. and Z.S. provided the bulk crystals. I.P., D.K., J.W. and G.S. interpreted the experimental and theoretical results. P.H., J.W. and G.S. wrote the manuscript, with contributions from all authors. All authors participated in the discussion and commented on the manuscript.

Competing interests

The authors declare no competing interests.

Additional information

Supplementary information The online version contains supplementary material available at https://doi.org/10.1038/s41566-024-01591-z.

Correspondence and requests for materials should be addressed to Giancarlo Soavi.

Peer review information *Nature Photonics* thanks Yi Wei Ho, Hongyuan Li, Zhipei Sun and the other, anonymous, reviewer(s) for their contribution to the peer review of this work.

Reprints and permissions information is available at www.nature.com/reprints.